Journal of the European Ceramic Society 36 (2016) 1033–1044

Contents lists available at www.sciencedirect.com

Journal of the European Ceramic Society

journal homepage: www.elsevier.com/locate/jeurceramsoc

Structural and magnetic properties of ceramics prepared by high-pressure high-temperature sintering of manganese-doped gallium nitride nanopowders☆

Mariusz Drygas[a], Jerzy F. Janik[a,*], Jacek Gosk[b], Stanislaw Gierlotka[c], Bogdan Palosz[c], Andrzej Twardowski[d,*]

[a] AGH University of Science and Technology, Faculty of Energy and Fuels, Al. Mickiewicza 30, 30-059 Krakow, Poland
[b] Warsaw University of Technology, Faculty of Physics, ul. Koszykowa 75, 00-662 Warszawa, Poland
[c] Institute of High Pressure Physics, Polish Academy of Sciences, ul. Sokołowska 29/37, 01-142 Warszawa, Poland
[d] University of Warsaw, Institute of Experimental Physics, Faculty of Physics, ul. Pasteura 2, 02-093 Warszawa, Poland

ARTICLE INFO

Article history:
Received 8 July 2015
Received in revised form 5 October 2015
Accepted 20 October 2015
Available online 11 November 2015

ABSTRACT

A precursor system made of $Ga(NMe_2)_3$ and $Mn[N(SiMe_3)_2]_2$ (Me = CH_3, initial Mn-contents 5, 10, 20 at.%) upon ammonolysis in refluxing ammonia afforded Ga/Mn amide-imide precursors. The 10 at.% Mn-precursor was nitrided at 500, 700, and 900 °C. The 5 and 20 at.% Mn-precursors were nitrided only at 900 °C. All nanopowders were characterized by XRD, FT-IR, SEM/EDX, whereas some by Raman spectroscopy and XRF. Magnetization measurements were performed with a SQUID magnetometer. Each nanopowder was subjected to no additive high-pressure high-temperature sintering, 7 GPa, 1000 °C, 10 min, affording ceramic pellets. Their structural and magnetic properties were examined to appraise an extent of Mn-incorporation into GaN under sintering conditions. In all samples, the paramagnetic phase of (Ga, Mn)N was accompanied by an antiferromagnetic residue, the latter resulting from oxidation of air sensitive Mn-excess by-products. (Ga, Mn)N in the ceramics showed increased Mn-contents about 1.6 times higher than in the parent nanopowders.

1. Introduction

Gallium nitride GaN doped with magnetic atoms such as Mn, Fe or Cr as well as other so-called diluted magnetic semiconductors have been in recent years a focus of extensive theoretical and experimental studies as prospective materials for spintronics [1]. However, the reported syntheses suffer from poor reproducibility whereas resulting materials appear to be far from anticipated solid solutions of suitably substituted metal centers and of targeted type of conductivity. Various kinetically stabilized by-products/precipitates/clusters/phases of unpredictable magnetic properties have been, instead, adventitiously formed pointing out to fundamental difficulties in extensive doping of the nitride's lattice with transition metals. That is also the experience of the authors of this report some of which contributed in the area of magnetic doping of thin films and monocrystals [2] whereas some researched Mn-doping of nanopowders [3]. In the latter area, a few new reports have been recently available including studies on (Ga, Mn)N nanopowders [4a,b], nanowires [4c], and nanorods [4d]. In this regard, a Mn-solubility in hexagonal GaN limited under selected conditions to mere 2.4 at.% is predicted from a calculated Ga–Mn–N phase diagram; the relatively low solubility is suggested to result from the Mn-incorporation into GaN losing competition with formation of a highly stable Mn_3GaN phase [5]. This result can be confronted with the reported/measured levels of Mn in GaN such as, for instance, 4.8 at.% for single crystals [6a], 7 at.% for nanopowders [6b] or even 10 at.% for nanowires [6c]. Given the specificity of nanostructures, one can anticipate the "nanosize stabilized", possibly increased proportions of incorporated Mn in nano-GaN, which is consistent with the relatively high Mn-contents in the cited cases. It needs to be underlined, though, that the analyzed Mn-contents do not have to be necessarily equivalent to Mn-incorporation in the substitutional (Ga, Mn)N.

Based on this experience, a new oxygen-free precursor system was recently devised and explored by us. The ammonolysis

☆ This paper is dedicated to Prof. Emer. Richard L. Wells, Duke University, Durham, North Carolina, USA on the occasion of his +80th birthday.

* Corresponding authors. Fax: +48 126342602.
E-mail addresses: janikj@agh.edu.pl (J.F. Janik), andrzej.twardowski@fuw.edu.pl (A. Twardowski).

http://dx.doi.org/10.1016/j.jeurceramsoc.2015.10.027
0955-2219/

in refluxing ammonia of the mixture of gallium tris(dimethyl) amide $Ga(NMe_2)_3$ and manganese bis(trimethylsilyl) amide $Mn[N(SiMe_3)_2]_2$ (Me = CH_3) followed by nitridation at elevated temperatures afforded bimetallic nanopowders build on the gallium nitride lattice [7]. The investigated precursor mixtures had the initial Mn-contents of 0.1, 5, 10, 20, and 50 at.%. Depending on processing conditions, up to a few percent of Mn were found to be incorporated in the GaN lattice forming the metal substituted (Ga, Mn)N. However, an incomplete transamination with ammonia of the bulky $Mn–N(SiMe_3)_2$ groups under the applied conditions of the synthesis resulted also in some contaminants formed from competing thermal decomposition of such groups. Among them, the residual amorphous Mn–N–Si–C species were found to be extremely reactive upon exposure to air and, eventually, yielded manganese silicate as a crystalline oxidation by-product. Some modifications of the synthesis method aimed at reducing amounts of the residual $N(SiMe_3)_2$ groups were thus advisable. Upon further exploring this issue we arrived at a conclusion that a two-stage nitridation in the system provided more structurally homogenous nanopowders, high Mn-contents in (Ga, Mn)N, and lower levels of retained $N(SiMe_3)_2$ groups compared with other routes [7]. In such a processing variant, a room temperature stabilized Ga/Mn amide-imide precursor is subjected under an ammonia flow, first, to a low temperature pyrolysis at 150 °C and, second, to a nitridation pyrolysis at elevated temperatures in the range 500–900 °C to yield the final nanopowders. This route was eventually employed in the current project.

Looking back at all the numerous yet unfulfilled attempts to incorporate sufficient manganese into the GaN lattice in the variety of materials forms and with various techniques that have been tried, one may consider the application of high-pressure high-temperature sintering of (Ga, Mn)N nanopowders as a promising means to achieve the goal. In this regard, high pressure may lead to new materials with unconventional physical, structural, and chemical properties [8]. The examples include studies on high-pressure high-temperature incorporation of Cr [9a] and Al [9b] in TiO_2.

If sintering is performed under conditions rendering (Ga, Mn)N powders to recrystallize, the applied pressure–temperature conditions could favor, on the one hand, Mn-incorporation and, on the other hand, advantageous phase separation of residual contaminants, if any. In this regard, we have demonstrated some time ago that no-additive sintering of GaN nanopowders could be achieved with or without significant grain recrystallization affording mechanically robust GaN pellets [10]. This by itself is quite characteristic for GaN among various nitrides since, for instance, silicon nitride Si_3N_4, aluminum nitride AlN or titanium nitride TiN powders seem to require liquid phase-forming additives to be sintered to high-density bodies [11a–d]. However, at least in the case of AlN and CrN nanopowders no-additive sintering was also reported [11e,f]. In this paper, described is a study on high-pressure high-temperature sintering of a range of (Ga, Mn)N nanopowders prepared by the ammonolysis in liquid ammonia of the bimetallic precursor system $Ga(NMe_2)_3/Mn[N(SiMe_3)_2]_2$ followed by a two-stage nitridation of the resulting precursors at elevated temperatures. Some excess of Mn compared to the known levels of Mn-incorporation in GaN was consciously applied with anticipated consequences of by-product formation and increased complexity of characterization data. It was presumed that the Mn-incorporation in the GaN lattice would initially take place along a specific chemical conversion pathway very much independently on the Mn excess-related decomposition side reactions and by-product formation during the nitridation step. Additionally, the sintering step could involve phase changes and recrystallization processes during which an available excess of Mn-content could come to play. Measurements of magnetization with temperature and field strength for the substrate powders and ceramic pellets were anticipated to help in the evaluation of various magnetic contributions and their structural basis.

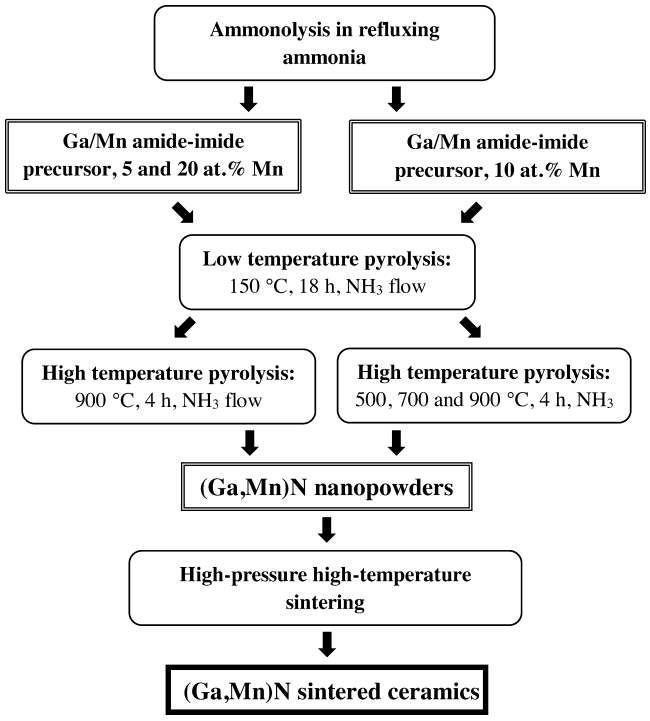

Fig. 1. Scheme of nitridation routes and sintering of (Ga, Mn)N nanopowders.

2. Experimental

2.1. Synthesis

The synthesis method used to make GaN/Mn powders was based on the anaerobic preparation of pure nanocrystalline gallium nitride GaN by ammonolysis of gallium tris(dimethyl) amide $Ga(NMe_2)_3$ (Me = CH_3) *via* the formation of gallium imide $\{Ga(NH)_{3/2}\}_n$ and nitriding pyrolysis of the latter at elevated temperatures [12]. In order to achieve the synthesis of Mn-doped materials, mixtures of $Ga(NMe_2)_3$ and $Mn[N(SiMe_3)_2]_2$ [13] with the predefined proportions of Mn/Ga at 5, 10, and 20 at.% Mn were first subjected to ammonolysis in refluxing/liquid ammonia followed by nitriding conversion as already reported [7]. In the present study, a two-stage pyrolysis under an ammonia flow, 0.5 L/min, of the Ga/Mn amide–imide precursor was applied: first stage at low temperature of 150 °C, 18 h and second stage at an elevated temperature, heating rate 5 °C/min, 4 h affording in all cases gray-beige to brownish final powders. For the initial 10 at.% Mn-precursor, the nitridation was carried out at 500, 700, and 900 °C to yield three respective products. For the 5 and 20 at.% Mn-precursors, only the 900 °C-treatment was carried out. The process stages and anticipated products are shown in Fig. 1.

2.2. Sintering

Five (Ga, Mn)N powders, that were prepared by the anaerobic synthesis, were sealed in glass vials under vacuum. Upon vial opening, the powders were removed and handled in air prior to the high-pressure high-temperature sintering using the methodology worked out earlier by some of us [10]. Specifically, the powders were sintered for 10 min in a high pressure torroid cell at 1000 °C under the pressure of 7 GPa yielding black ceramic pellets, D = 4 mm, thickness 1–2 mm (Fig. 2). The pellet that was made from

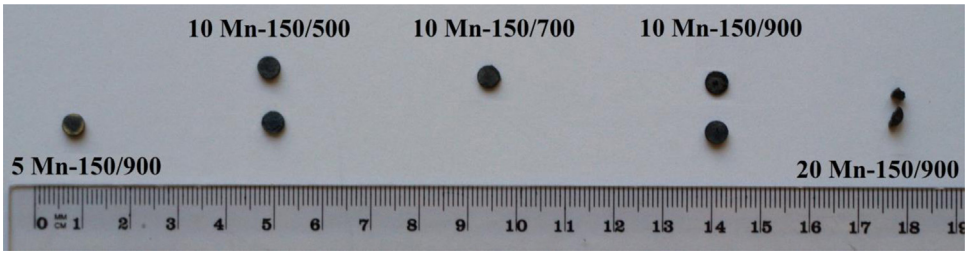

Fig. 2. Snapshot of the sintered pellets.

powder with the initial 5 at.% Mn-content, which was pyrolyzed in the second-stage at 900 °C, was optically inhomogeneous having a slight beige rim on its surface (Fig. 2, first from the left).

2.3. Sample labeling

The samples were labeled to show the important synthesis parameters, *i.e.*, the Mn-content and second-stage pyrolysis temperature. For example, the label 10Mn-150/900 refers to the powder prepared from the bimetallic precursor containing initially 10 at.% Mn and pyrolyzed first at 150 °C followed by nitridation at 900 °C. The following five samples were thus prepared and, subsequently, sintered: 10Mn-150/500, 10Mn-150/700, 10Mn-150/900, 5Mn-150/900, and 20Mn-150/900. The series of the first three powders was intended to study the impact of nitridation temperature at the fixed 10 at.% Mn-content whereas the remaining two powders, *i.e.*, 5Mn-150/900 and 20Mn-150/900 combined with 10Mn-150/900 enabled to study the impact of the initial Mn-contents, *i.e.*, 5, 10, and 20 at.%, at the fixed nitridation temperature of 900 °C. The sintered sample names were preceded by ceram, *e.g.*, ceram10Mn-150/700 was the ceramics sintered from nanopowder 10Mn-150/700.

2.4. Characterization

Product powders were characterized by the powder XRD technique with an Empyrean (PANalytical) diffractometer (Cu Kα source; $2\theta = 20–80^{\circ}$). Average crystallite sizes were evaluated from the Scherrer's equation applying the Rietveld refinement method (HighScore Plus by PANalytical). FT-IR spectra (KBr pellets) were collected on a Nicolet 380 spectrometer. SEM/EDX study was performed using a Hitachi Model S-4700 scanning electron microscope. Magnetization of the samples was measured as a function of magnetic field (up to 7 T) and temperature (2–400 K) using a SQUID magnetometer. The powder samples were placed in gelatin capsules showing controlled diamagnetic signal. To reduce the ratio of the capsule signal to signal of the measured sample, the sample mass was maximized with respect to the upper limit of the SQUID operation range.

3. Results and discussion

The ammonolysis and nitridation chemistry in the bimetallic system made of gallium tris(dimethyl) amide $Ga(NMe_2)_3$ and manganese bis(trimethylsilyl) amide $Mn[N(SiMe_3)_2]_2$, Me = CH_3, relies on transamination of the organic amide groups with ammonia and on thermally driven multistep elimination/condensation of the resulting $—NH_2$ and $=NH$ groups towards metal nitride lattices. In a somewhat simplified way, one can sketch that with increasing temperatures the following reaction sequence takes place: $Ga(NMe_2)_3 + 3NH_3 \rightarrow Ga(NH_2)_3$ (amide) $+ \uparrow 3HNMe_2 \rightarrow Ga(NH)_{3/2}$ (imide) $+ \uparrow 3/2NH_3 \rightarrow GaN$ (nitride) $+ \uparrow 1/2NH_3$ [12]. Theoretically, a similar pathway could be envisioned also for a divalent Mn (II)-derivative but the relevant manganese bis(dimethyl) amide $Mn(NMe_2)_2$ is unknown and our initial attempts to synthesize it so far have failed to reach the goal. That was the reason to use, instead, the available manganese bis(trimethylsilyl) amide [13]. Our related study on the individual ammonolysis of this precursor confirmed such transamination/deamination processes to proceed in refluxing ammonia with the formation of nanocrystalline η-Mn_3N_2 already upon nitriding pyrolysis at 150 °C [unpublished].

Deamination reactions in the binary metal amide system could, arguably, result in intermolecular coupling processes of the type $Ga–NH_2 + [(Me_3Si)_2N]–Mn \rightarrow Ga–N(H)–Mn + \uparrow H[N(SiMe_3)_2]$ or according to $Ga\text{-}NH_2 + H_2N–Mn \rightarrow Ga–N(H)–Mn + \uparrow NH_3$ resulting in mixed metal–nitrogen bond formation. This is feasible due to fast transamination of $Ga–NMe_2$ to reactive $Ga–NH_2$ species followed by deamination and gallium imide $\{Ga(NH)_{3/2}\}$ formation already at room temperature [12] and equally efficient $Mn–NH_2$ formation under comparable conditions. Additional credentials for this are lent from an earlier study on the system gallium tris(dimethyl) amide/aluminum tris(dimethyl) amide which upon reactions with ammonia and pyrolysis afforded solid solutions of (Ga, Al)N [12b].

Admittedly, composition limits of the target substitutional (Ga, Mn)N phase and its stability at extreme pressures and elevated temperatures during the second phase of the project, *i.e.*, sintering of Mn-doped nanopowders are unknown. In the case of the likely increased Mn-incorporation into reforming GaN lattices compared to the composition of the substrate (Ga, Mn)N nanopowder,

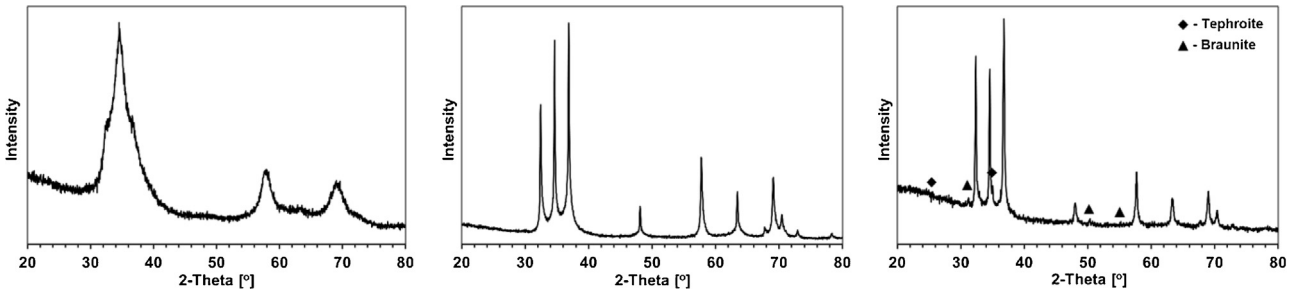

Fig. 3. XRD patterns for selected (Ga, Mn)N powders: left—5Mn-150/900, middle—10Mn-150/900, right—20Mn-150/900.

Table 1
Crystallographic data and average crystallite sizes estimated from XRD patterns for nanopowders. c-GaN and h-GaN indicate the structure type of GaN-based lattices; n/d—not determined.

Final nitridation temperature	Sample	Phase: content [%]	Lattice parameters [Å]	Average crystallite size D [nm]
500 °C	10Mn-150/500	highly amorphous powder on the verge of crystallinity	n/d	n/d
700 °C	10Mn-150/700	c-GaN (large nano): 6	$a = 4.54$	43
		h-GaN (small nano I): 55	$a = 3.21$ $c = 5.22$	8
		h-GaN (small nano II): 39	$a = 3.17$ $c = 5.92$	2
900 °C	10Mn-150/900	h-GaN (large nano): 37	$a = 3.19$ $c = 5.19$	60
		h-GaN (small nano): 63	$a = 3.19$ $c = 5.19$	5
900 °C	5Mn-150/900	c-GaN: 52	$a = 4.52$	4
		h-GaN: 48	$a = 3.20$ $c = 5.30$	3
900 °C	20Mn-150/900	h-GaN: 89	$a = 3.20$ $c = 5.19$	35
		Tephroite, Mn_2SiO_4: 8 (Pnma)	$a = 10.59$ $b = 6.27$ $c = 4.90$	>200
		Braunite, $Mn^{2+}Mn^{3+}{}_6SiO_{12}$: 3 (I41/acd)	$a = 9.43$ $c = 18.77$	>200

some excess of manganese was needed. Purposely applied excessive quantities of manganese precursor, which we used in the synthesis of nanopowders, were intended to provide such a readily available, mixed on the nanosize level Mn-source.

3.1. Characterization of substrate nanopowders

The nanopowders prepared *via* various synthesis routes shown in Fig. 1 were extensively investigated and their characterization was reported elsewhere [7]. Below, the specific XRD and magnetic determinations will be discussed in details to illustrate from this angle the materials characteristics.

3.1.1. Powder XRD diffraction

As a representative example, Fig. 3 shows the XRD patterns for three products from nitridation at 900 °C. Table 1 includes the structure type and particle size parameters derived from the patterns for all five nanopowders.

The data pointed out to the major GaN lattice-based phases in all nanopowders. The XRD pattern for 10Mn-150/500 was typical for an amorphous substance on the verge of crystallinity with barely discernible broad halos [14]. Two patterns, 10Mn-150/700 and 5Mn-150/900, were best fitted assuming in each case a certain proportion of the cubic polytype c-GaN in addition to the hexagonal polytype h-GaN. This was rather unexpected, especially for the 5Mn-150/900 product from the relatively high nitridation temperature of 900 °C, to detect c-GaN after all. A characteristic feature of the patterns for 10Mn-150/700 and 10Mn-150/900 was an unusual broadening of peak bases, which was tentatively attributed to multimodal size distribution, *i.e.*, the presence of larger crystallites and smaller ones that belonged to two or more size distribution modes in the low nanosized range (Table 1; large nano, small nano). Such an argument found support from the relevant SEM data [7]. However, there are more complex explanations possible, too, including specific lattice disorders due to small cubic domains incorporated in the predominantly hexagonal GaN-type lattice as well as texturing effects that could also be invoked but they are beyond the scope of this study. The structure and size parameters shown in Table 1 are intended to be merely consistent approximations pointing out to trends and affording relative comparisons whereas not allowing strict quantitative assessments. For 20Mn-150/900, two manganese silicate polytypes, tephroite (orthorhombic Pnma) and braunite (tetragonal I41/acd), were identified in very small quantities in addition to major GaN. They are thought to be adventitious oxidation products of either the postulated transient manganese silicon nitride [15] or amorphous Mn–N–Si–C-type of species that were formed *via* thermal decomposition of residual Mn-N$(SiMe_3)_2$ groups. In this regard, the nanopowders with the highest initial quantities of the manganese precursor, which were prepared under strict anaerobic conditions, were occasionally seen smoking upon exposure to air consistent with facile oxidation of the Mn-containing by-products.

3.1.2. Magnetization measurements for nanopowders

Magnetization M was measured as a function of magnetic field B up to 7 T at different temperatures and as a function of temperature, $2\,K < T < 400\,K$, at the constant field $B = 1$ T. In general, all measured samples showed both the paramagnetic PM and antiferromagnetic AFM contributions whereas there was no evidence for ferromagnetic FM precipitates/clusters. The representative results of the M *vs.* B data for two selected nanopowders 10Mn-150/700 and 20Mn-150/900 are shown in Fig. 4.

Magnetization of both samples reveals rather typical paramagnetic, Brillouin-like behavior: it tends to saturate with increasing magnetic field at the lowest temperatures whereas at higher temperatures ($T \geq 50\,K$) it is practically linear with magnetic field. However, we note that magnetization saturates much slower with increasing magnetic field than expected for non-interacting Mn-ions (*cf.* magnetization at $T = 2$ K and appropriate Brillouin function for $T = 2$ K in Fig. 4). The slower than expected saturation may result from AFM interactions between Mn-ions in the (Ga, Mn)N phase and/or some additional linear contribution from the antiferromagnetic phase present in the samples. Another piece of evidence of AFM interactions between Mn-ions in (Ga, Mn)N is provided if measured magnetization is plotted as a function of B/T (not shown). In the low temperature range (2, 5, 10, 30, and 50 K), the M *vs.* B/T curves do not collapse in one curve which should be the case of non-interacting magnetic moments. Based on our earlier studies, we ascribe the observed AFM behavior to result from both the AFM interactions between Mn-ions of (Ga, Mn)N and the presence of antiferromagnetic Mn_2SiO_4 [7].

The contribution of the (Ga, Mn)N phase can be extracted from a total measured magnetization if AFM interaction strengths (exchange constants) are pronouncedly different in the (Ga, Mn)N

Table 2
Estimated Mn-contents in the paramagnetic phase (Ga, Mn)N (at.%) and the contents of residual antiferromagnetic Mn_2SiO_4 (wt.%) in nanopowders; n/d—not determined; * shows the data for a sample from one-stage nitridation.

	10Mn-150/500	10Mn-150/700	10Mn-150/900	5Mn-150/900	5Mn-900*	20Mn-150/900
Mn-content in (Ga, Mn)N [at.%]	>2.2	3.2	>1.7	n/d	2.1*	>2.3
wt.(Mn_2SiO_4)/wt. (sample) × 100% [wt.%]	8.3	8.1	5.7	n/d	1.4*	5.8

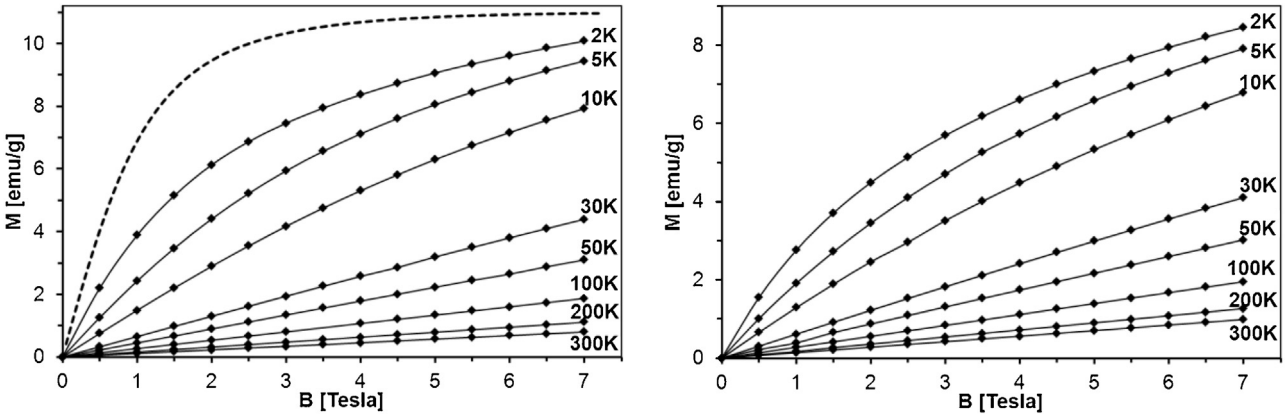

Fig. 4. Magnetization as a function of magnetic field at different temperatures for: left—10Mn-150/700; dashed line represents a selected Brillouin function with $S = 5/2$ for a theoretical Mn-content of 3.2 at.%; right—20 Mn-150/900. For 20Mn-150/900, a higher AFM contribution and a lower total magnetization should be noticed.

and AFM phase(s) since, in such a case, the paramagnetic (Ga, Mn)N and the AFM phase(s) show distinct magnetic behavior. The procedure is described in details in our previous work [7]. The result of subtraction of the AFM phase contribution from the total magnetization is depicted in Fig. 5, where $M_{total} \times T$ *vs.* T and $M_{GaMnN} \times T$ *vs.* T are shown. In Fig. 5, left panel, the curves are numbered consecutively with increased total magnetization and this curve/sample numbering scheme is retained in the right panel. In this series, there is no available measurement for sample 5Mn-150/900 and, instead, as a decent approximation of the missing data the results for related powder 5Mn-900 from one-stage pyrolysis are included and labeled with asterisk. As before, a dominant antiferromagnetic contribution due to Mn_2SiO_4 is assumed.

From the high temperature data of $M_{GaMnN} \times T$ *vs.* T, where the curves are horizontal, the concentration of Mn in the (Ga, Mn)N phase for each sample can be estimated (provided the mass of the residual by-products is evaluated or neglected as for 10Mn-150/700). For 10Mn-150/900, a concave shape of the curve suggests some additional AFM contribution other than Mn_2SiO_4. We note that sample 20Mn-150/900 shows a much larger AFM contribution to the total magnetization than sample 10Mn-150/700 as evidenced in Figs. 4 and 5. The antiferromagnetic contributions of Mn_2SiO_4 and the estimated Mn-contents in (Ga, Mn)N are collected in Table 2 that includes also the data for 5Mn-900 from one-stage pyrolysis that are labeled with asterisk. One should keep in mind that for 10Mn-150/500 and 10Mn-150/900 only upper weight limits can be determined so the estimated Mn-concentrations represent the lower limit of x.

As commonly used in the relevant literature, the substitutional Mn-contents are expressed in at.% to relate them directly to the number of Ga-centers in the GaN lattice. These contents refer to the separate magnetic phase of (Ga, Mn)N and, therefore, are conceptually independent on the nanopowders component composition. On the other hand, the Mn_2SiO_4-contents are expressed in wt.% as a customary way of showing the composition of mixtures. A more coherent and comprehensive appraisal of manganese distribution among various components could not be done because of the presence of unspecified quantities of amorphous polymeric N–Si–C residues that may include some manganes, too. The limit is that all these Mn-contributions together do not exceed the initial Mn-content in the precursor mixture.

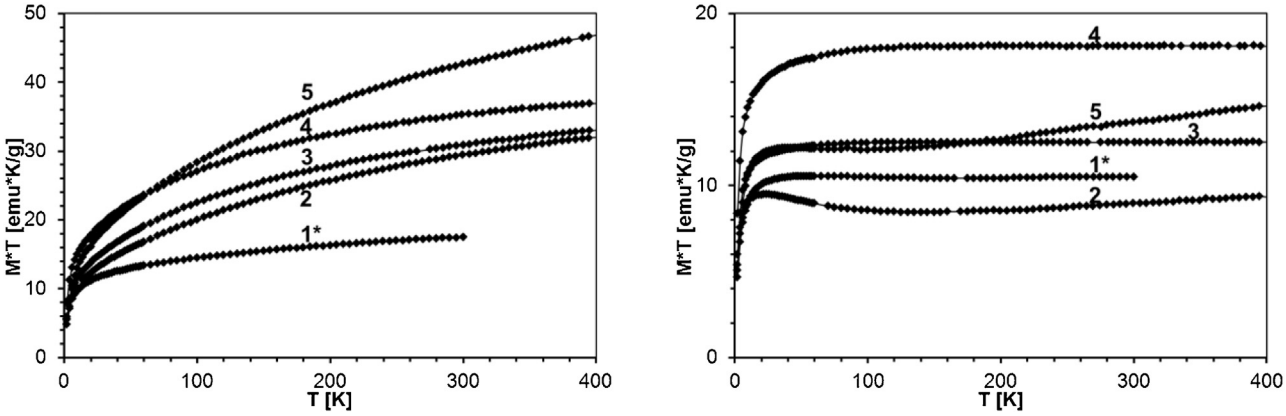

Fig. 5. $M \times T$ as a function of T at $B = 1$ T for nanopowders 1–5. Left—total magnetization for the as-measured samples (both PM and AFM contributions); right—after subtraction of AFM contribution. 1*–5Mn-900, 2–10Mn-150/900, 3–10Mn-150/500, 4–10Mn-150/700, 5–20Mn-150/900.

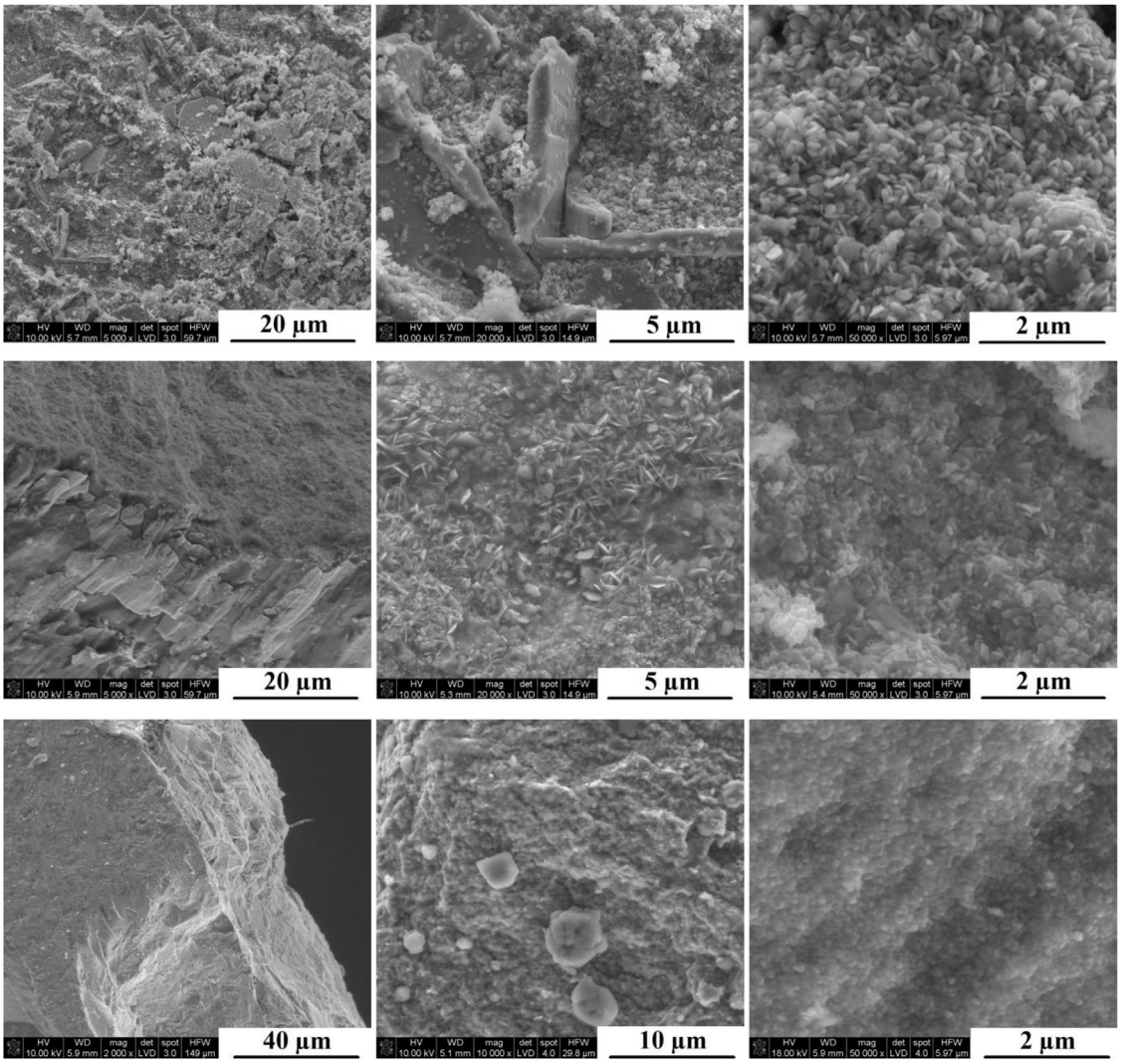

Fig. 6. SEM images of fractures for sintered (Ga, Mn)N ceramics: top row—ceram10Mn-150/500, middle row—ceram10Mn-150/700, bottom row—ceram10Mn-150/900.

3.1.3. Summary of nanopowder characteristics

The nanopowders were found to be mixtures of the prevailing crystalline Mn-doped (Ga, Mn)N target phase and the minor amorphous Mn–N–Si–C-type of an ill-defined by-product. The latter originated from a persistently incomplete ammonolysis stage of the synthesis, which was enhanced by the purposely applied excess of manganese precursor. The by-product that was detected in various quantities by such analytical methods as XRF, FT-IR, Raman, and SEM/EDX appeared to be amorphous even after the highest applied nitridation temperature of 900 °C [7]. It showed to be highly reactive during its essential handling in air. Upon oxidation it yielded in part the crystaline manganese silicates and, mostly, other amorphous by-products, likely, N–Si–C polymeric species of which presence was found chemically neutral to the stability and properties of (Ga, Mn)N. It needs to be reiterated that the entire synthesis was done under strict anaerobic conditions whereas subsequent characterization steps and sample preparation for sintering, occasionally, required some exposure to air. Keeping this in mind, suitably adjusted handling procedures in many cases could eliminate/reduce the oxidation by-products.

At this point, we are quite convinced that sufficiently long times of ammonolysis (several tens of hours) at or below *ca.* 150 °C coupled with higher ammonia gas flows could remedy the problem of the by-product formation. Such an approach, however, was impractical in the original study given a multitude of reaction pathways/variations that were applied in the synthesis of the nanopowders [7]. At the end, this added to a complexity of the following nitridation stage and the characterization efforts afterwards but still enabled the identification and investigation of the target (Ga, Mn)N phase.

3.2. Sintering study

The (Ga, Mn)N nanopowders for sintering study included a subset of three powders that were related by the same initial 10 at.% Mn-content whereas being nitrided at three different temperatures and a subset of three powders that were related by the same pyrolysis temperature of 900 °C whereas originating from three different initial Mn-contents. They all were prepared from the 150 °C-pyrolyzed precursors (Fig. 1), which assured at the start the lowest amounts of the residual Mn-N$(SiMe_3)_2$ groups among other conversion options. It was hoped, anyway, that the small quantities of the residuals, by playing a secondary and possibly neutral role, would not decisively impact the chemistry of the target Mn-doping of GaN. The high oxidation affinity of the by-products was another fact of life but if understood correctly might not interfere with the magnetic properties of the predominant GaN-based matrix. Eventually, mechanically robust black pellets were obtained confirming the ability to sinter GaN-based nanopowders without additives. The applied high-pressure high-temperature sintering conditions

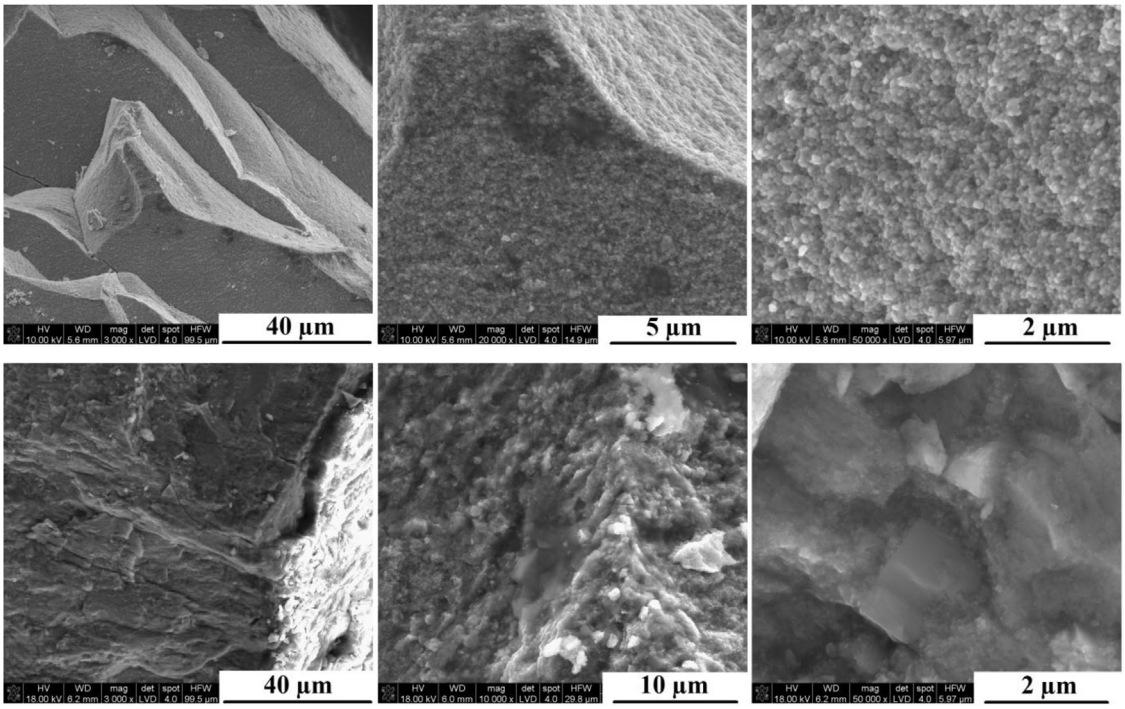

Fig. 7. SEM images of fractures for sintered (Ga, Mn)N ceramics: upper row—ceram5Mn-150/900, lower row—ceram20Mn-150/900.

were extreme and expected to result in grain recrystallization. Such a course of events should drastically influence the conditions of Mn-incorporation into the *in-situ* reforming GaN lattices.

3.2.1. SEM examination of ceramics

The SEM images of ceramics fractures for the 10 at.% Mn precursor-derived materials, *i.e.*, ceram10Mn-150/500, ceram10Mn-150/700, and ceram10Mn-150/900 are shown in Fig. 6.

The set of three images in Fig. 6, top row, for ceram10Mn-150/500 shows it to be made of surprisingly uniform hexagonal platelets with the thickness of several tens and the diameter of a few hundreds of nanometers, which form a ceramic matrix. There are also quite a few blocky plates that are immersed in the matrix, which are analyzed by EDX as composed prevailingly of gallium Ga and oxygen O suggesting gallium oxide. A few other chunks are found enriched in Mn and Si. This suggest a mixture of various components.

The analysis of three images in the middle row for ceram10Mn-150/700 supports an overall grainy morphology of the matrix with distinct areas containing very thin platelets, although of different habit than observed earlier for ceram10Mn-150/500. The latter are found by EDX to be enriched in Si and Mn. Although not shown in the pictures, occasionally, rounded amorphous features are also seen that by EDX seem to be made of carbon C.

The images in the bottom row for ceram10Mn-150/900 appear to show the most homogeneous compact structure among the ones just discussed. The predominant grainy morphology of the matrix (bottom row, right) seems to be only very rarely disturbed by intrusions of larger grain clusters or amorphous chunks (bottom row, middle) that are analyzed by EDX as mostly composed of C. The EDX scanning of the matrix provides with the uniform element distribution for Ga, Mn, and N.

Fig. 7 shows the SEM pictures for two remaining ceramics, namely, ceram5Mn-150/900 (upper row) and ceram20-150/900 (lower row), which are interesting to compare with the ceram10Mn-150/900 discussed in the previous paragraph. Ceram5Mn-150/900 displays, in general, a uniform grainy morphology that is "decorated" at times with dark to black spots (upper row, left and middle). Some of the thicker layers of this type are analyzed by EDX as enriched in Si and, possibly, Mn. A rather unexpected feature for ceram20Mn-150/900 is a very fine grain nature of the matrix (Fig. 7, lower row, right) that looks much finer than seen previously for ceram5Mn-150/900. There are also much larger blocky crystallites embedded in the matrix that are enriched in Si and Mn as well as occasional flat amorphous layers analyzed as C. In general, all ceramics made from 900 °C-pyrolyzed powders are similar to each other and show the homogeneous and compact structures. They appear to be composed of the matrices made of quite uniform nanograins that host some individual inclusions including Si and Mn enriched phases and amorphous C.

3.2.2. XRD patterns for ceramics

The XRD patterns for all five ceramics are included in Fig. 8. There are two patterns shown for ceram10Mn-150/700 which are enclosed in the rectangular box. The pattern for the original pellet is on the left side in the box and includes a few very low intensity peaks at 2θ *ca.* 20–23° of surface contaminants that were suspected to originate from sintering process. The pellet was then mechanically polished and the second pattern was obtained (right in the box) which no longer contained the contaminants. The essential structure and size parameters calculated from the patterns are shown in Table 3. It is worth to note that the calculated average crystallite sizes tend to underestimate proportions of the large crystallites with $D > 150$–200 nm, which do not contribute to a size-related peak width. As a general rule, we use average crystallite sizes of a related pool of nanomaterials mainly for comparative purposes and trend identification with utmost care paid to their absolute values. This is especially true if pronounced crystal texturing and internal stress come to play as in the case of the sintered materials.

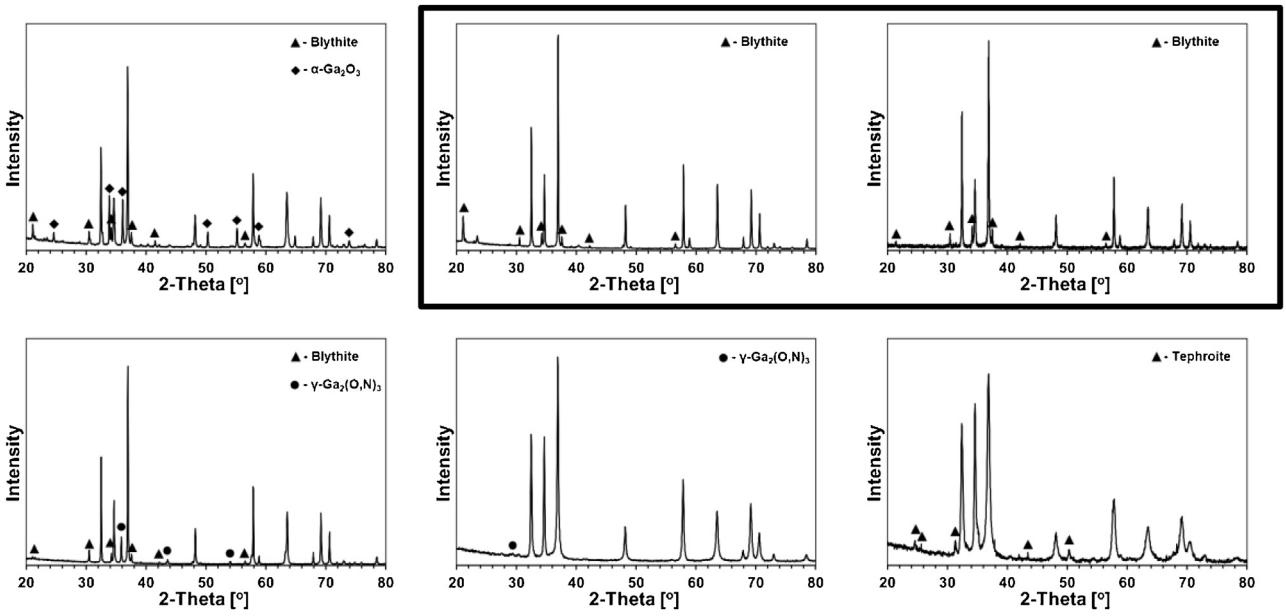

Fig. 8. XRD patterns of ceramics: top left—ceram10Mn-150/500, top frame: left panel—raw ceram10Mn-150/700, right panel—polished ceram10Mn-150/700, bottom left—ceram5Mn-150/900, bottom middle—ceram10Mn-150/900, bottom right—ceram20Mn-150/900.

Table 3
Crystallographic data and average crystallite sizes estimated from XRD patterns for (Ga, Mn)N ceramics; n/d—not determined.

	Phase(space group), formula: content [%]	Lattice parameters [Å]	Average crystallite size *D* [nm]
ceram10Mn-150/500	h-GaN($P6_3mc$): 67	$a = 3.19$ $c = 5.19$	85
	α-Ga_2O_3(R-3c): 23	$a = 4.98$ $c = 14.34$	85
	Blythite(Ia-3d), $Mn_3^{2+}Mn_2^{3+}(SiO_4)_3$: 10	$a = 11.75$	>200
ceram10Mn-150/700	h-GaN($P6_3mc$): 81	$a = 3.19$ $c = 5.19$	75
	Blythite(Ia-3d), $Mn_3^{2+}Mn_2^{3+}(SiO_4)_3$: 19	$a = 11.75$	>200
ceram5Mn-150/900	h-GaN($P6_3mc$): 79	$a = 3.19$ $c = 5.19$	>200
	Blythite(Ia-3d), $Mn_3^{2+}Mn_2^{3+}(SiO_4)_3$: 6	$a = 11.75$	>200
	γ-$Ga_2(O,N)_3$(Fd-3m): 15	$a = 8.32$	70
ceram10Mn-150/900	h-GaN($P6_3mc$): 99	$a = 3.19$ $c = 5.19$	40
	γ-$Ga_2(O,N)_3$(Fd-3m): 1	$a = 8.35$	n/d
ceram20Mn-150/900	h-GaN($P6_3mc$): 91	$a = 3.19$ $c = 5.19$	20
	Tephroite(Pnma), Mn_2SiO_4: 9	$a = 10.55$ $b = 6.29$ $c = 4.90$	>200

The applied sintering pressure–temperature conditions, 7 GP and 1000 °C, were extreme enough to cause grain recrystallization and conversion of the metastable c-GaN to the stable h-GaN. In general, this is confirmed for all of the sintered powders but some specific cases need to be underlined. For 10Mn-150/500, the sintering causes the initially amorphous powder (see, Table 1) to recrystallize to GaN grains in the upper nanosized regime with hexagonal platelet morphology (Fig. 6). Some α-Ga_2O_3 and blythite $Mn_3^{2+}Mn_2^{3+}(SiO_4)_3$ are also present. The latter is a high pressure-formed mineral that was previously observed upon application of 1000 °C and 9 GPa to mixtures of manganese and silicon oxides [16], the circumstances close to the sintering conditions in this study. In the related high pressure experiments, tephroite, yet another manganese silicate was observed as well. The presence of blythite is consistent with the amorphous $MnSiN_2$ or Mn–N–Si–C by-products in the starting powder (Fig. 3), which apparently underwent a facile oxidation upon exposure to air during sample manipulations. The high oxidation affinity of this relatively low temperature-pyrolyzed powder (500 °C) is reflected also in the presence of some gallium oxide in the pellet. In conclusion, the major drawback in studying this highly amorphous material stems from its high reactivity due to high surface area and the presence of reactive by-products.

The complex mixture of gallium nitride polytypes with multimodal size distributions, which was initially present in powder 10Mn-150/700 (Fig. 3, Table 1), was converted upon sintering to the single h-GaN phase with uniform grain morphology (Fig. 6). The occurrence of some blythite is thought to originate from the same decomposition pathway of the by-products as previously described. Since no crystalline oxide-type components were detected by XRD in the starting powder, the by-product oxida-

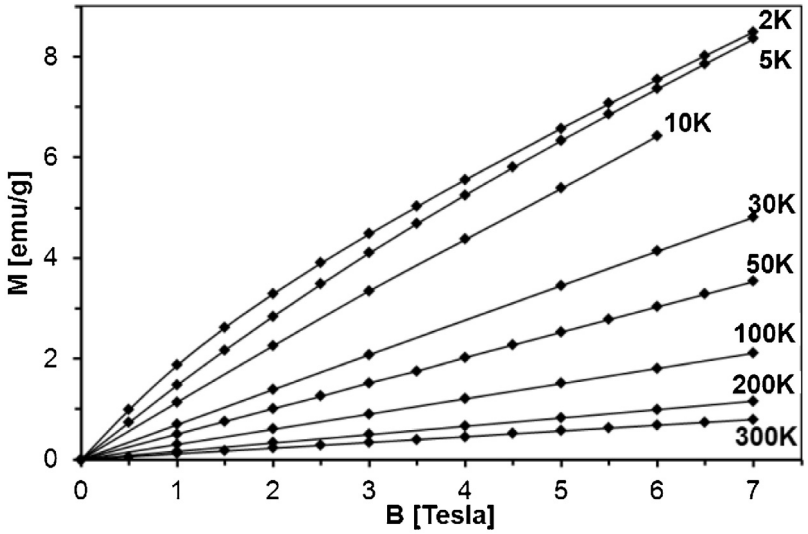

Fig. 9. Magnetization M of ceram10Mn-150/700 as a function of magnetic field B for different temperatures.

tion likely took place during sample handling and manipulations prior sintering. The 700 °C-derived powder appears to be reactive in air, although to a lesser degree than the earlier discussed 500 °C-derived powder.

The sintering of 5Mn-150/900 that was initially a mixture of c-GaN and h-GaN with the average crystallite sizes of a few nanometers (Fig. 3, Table 1) afforded the single h-GaN polytype recrystallized to crystallite sizes >200 nm. These gallium nitride crystallites form a uniform grainy morphology of the ceramics with occasional inclusions (Fig. 7). The presence of some blythite supports, again, the high oxidation affinity of the amorphous by-products. Interestingly, there is also a new phase of spinel-type that is similar to the reported γ-Ga_2O_3 [17a] whereas differing significantly with lattice parameters pointing out to gallium oxynitride spinel $Ga_2(O,N)_3$. The formation of $Ga_2(O,N)_3$ in the nanopowder form is still disputable but its formation was both theoretically predicted and experimentally proven in high pressure reactions of gallium oxide and gallium nitride [17b–d]. It is plausible that the presence of Mn and Si could have promoted the spinel formation and stabilization.

The most phase homogenous in the series is the ceramics from 10Mn-150/900 that is composed predominantly of h-GaN (99%) with 40 nm average crystallite size. It originated from the initial powder with the bimodal size distribution of h-GaN, $D = 5$ and 60 nm (Table 1), pointing out to recrystallization of the finest grain fractions. There are only traces (<1%) of the $Ga_2(O,N)_3$ spinel phase at the limits of detection. It is worth to recall, however, that SEM/EDX analysis pointed out to some amorphous carbon inclusions that are also present (Fig. 6).

The highest initial Mn-content ceramics made from 20Mn-150/900 is also quite phase homogeneous containing 89% of h-GaN and 11% of the high-pressure stable tephroite, not much of a surprise, since the manganese silicates tephroite and braunite were analyzed in the substrate powder, anyway. Perhaps the most unexpected is the relatively low average crystallite size of h-GaN, $D = 20$ nm, to be compared with this size for h-GaN in the starting powder, $D = 35$ nm. Somewhat against the trend and intuition, this ceramics is made of the crystallites that are clearly smaller on average than the ones in the starting nanopowder before sintering.

3.2.3. Magnetic measurements for ceramics

The magnetic behavior of all sintered ceramics is quite different from that of the substrate nanopowders. It is well exemplified by magnetization data for the sintered sample of ceram10Mn-150/700 shown in Figs. 9 and 10.

Comparing the data for the substrate nanopowder and the sintered ceramics derived from it one notes that while the high temperature data are essentially quite similar for both samples, the low temperature magnetization of the sintered sample saturates with magnetic field much more slowly than that of the parent nanopowder (*cf.* data at low temperatures, especially for $T = 2$ K in Figs. 4 and 9). This may result from stronger Mn–Mn AFM interactions in (Ga, Mn)N or a higher contribution of the AFM phase(s) in total magnetization. Since the high temperature data are very similar for both samples (*cf.* data for $T = 50$, 100, 200, and 300 K in Figs. 4 and 9), the low temperature difference may be due to a stronger effect of Mn–Mn interactions, which in turn may suggest a higher Mn-concentration in the sintered ceramics. We recall that the Mn–Mn interaction effects observed in magnetization increase with increasing Mn-concentrations for the constant Mn-concentration independent Mn–Mn exchange integral.

The above observation is further supported by data illustrated in Fig. 10 where $M \times T$ *vs.* T are shown for nanopowder 10Mn-150/700 and sintered ceram10Mn-150/700. The right panel shows a comparison of the normalized/scaled curves $M \times T$ *vs.* T for the nanopowder and the related ceramics. For the latter, a stronger downward bending of $M \times T$ is encountered (pointing out to a stronger AFM effect) whereas the larger values of $M \times T$ at higher temperatures, where $M \times T$ *vs.* T is horizontal, indicate a relatively higher Mn-concentration.

Fig. 11 includes the data for all sintered samples: left panel—as measured, right panel—corrected for the AFM phase of Mn_2SiO_4. The curve numbering is the same as applied earlier for the parent nanopowders in Fig. 5, *e.g.*, curve 4 is for nanopowder 10Mn-150/700 in Fig. 5 and for the derived from it sintered material of ceram10Mn-150/700 in Fig. 11, *etc*. Among the five sintered samples, ceram10Mn-150/700 shows the highest PM contribution whereas its AFM contribution is among the lowest ones (Fig. 11, right and Fig. 10, left, respectively). The overall lowest PM contribution is found for ceram20Mn-150/900 that, at the same time, is characteristic of the highest AFM contribution among all ceramics. This parallels the characteristics of parent nanopowder 20Mn-150/900 in relation to other powders. A detailed analysis of the $M \times T$ *vs.* T curves, including the relevant literature data [18], was consistent with the latter contribution being due to Mn_2SiO_4. However, there are indications (curve concavity) for an additional magnetic

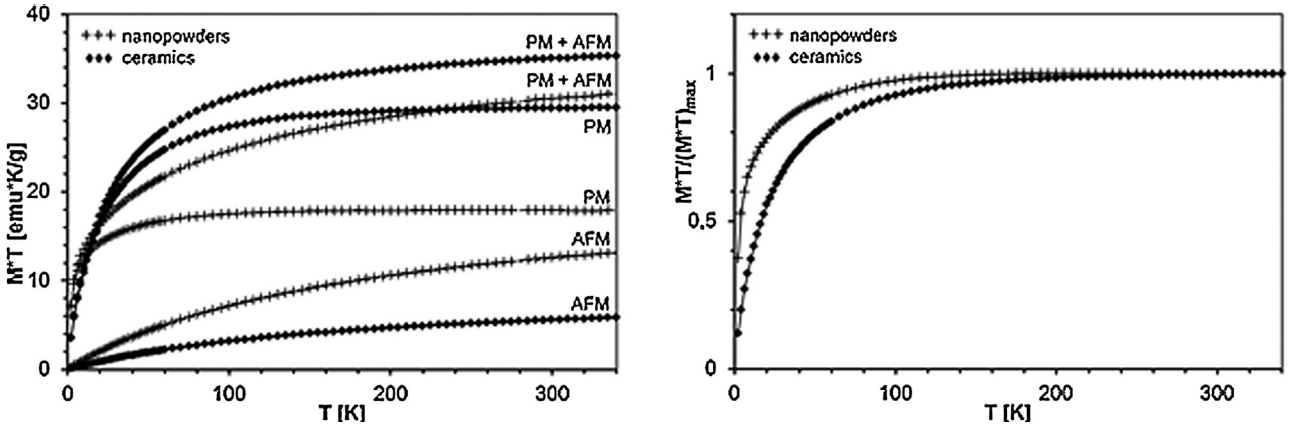

Fig. 10. Left—$M \times T$ *vs. T* curves at $B = 1$ Tesla for nanopowder 10Mn-150/700 (diamonds) and related sintered ceram10Mn-150/700 (plus signs). Magnetization curves for: AFM + PM—total/measured magnetization, *i.e*, antiferromagnetic + paramagnetic contributions; PM—paramagnetic contribution, *i.e.*, after subtraction of AFM contribution due to Mn_2SiO_4 from total magnetization; AFM—antiferromagnetic contribution due to Mn_2SiO_4. Right—normalized PM contributions $M_{PM} \times T/(M_{PM} \times T)_{max}$ in (Ga, Mn)N showing stronger AFM interactions in ceram10 Mn-150/700.

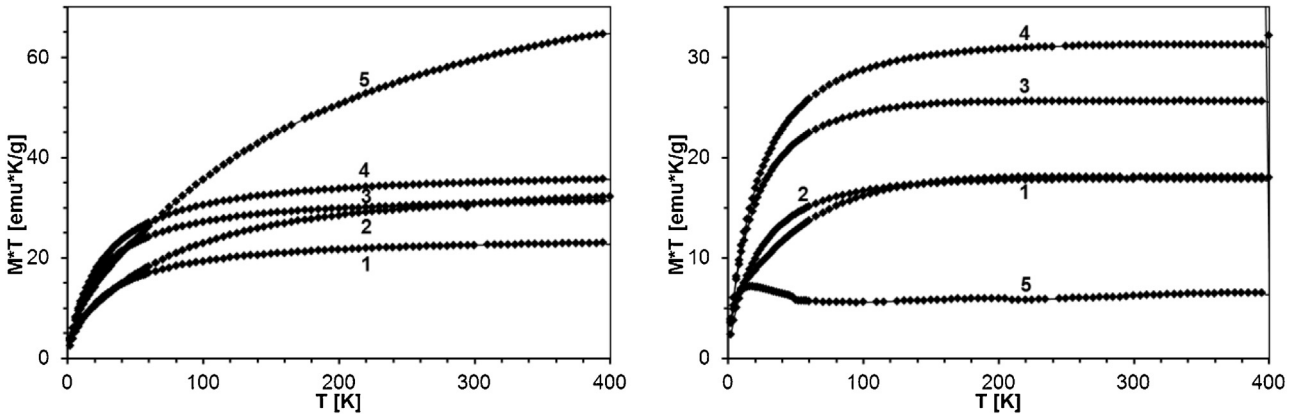

Fig. 11. $M \times T$ *vs. T* at $B = 1$ Tesla for sintered ceramics 1–5. Lef—M(AFM + PM) $\times$ *T* (as measured) *vs. T*; right—*M*(PM) $\times$ *T vs. T* (after subtraction of AFM contribution due to Mn_2SiO_4). 1—ceram5Mn-150/900, 2—ceram10Mn-150/900, 3—ceram10Mn-150/500, 4—ceram10Mn-150/700, 5—ceram20 Mn-150/900.

Table 4
Contents of Mn in paramagnetic (Ga, Mn)N, of antiferromagnetic Mn_2SiO_4 by-product, and of diamagnetic phases in the sintered ceramics.

	ceram10M-150/500	ceram10M-150/700	ceram10M-150/900	ceram5Mn-150/900	ceram20M-150/900
Mn-content in (Ga, Mn)N [at.%]	>4.5	5.5	3.2	>3.1	1.6
wt.(Mn_2SiO_4)/wt.(sample) $\times$ 100% [wt.%]	2.4	1.3	5.9	1.9	21
Diamagnetic	α-Ga_2O_3	–	γ-$Ga_2(O,N)_3$	γ-$Ga_2(O,N)_3$	–
phase	23		1	15	
[wt.%]					

by-product in this ceramics. Finally, we note a *ca.* 5-fold increase of the PM contribution when going from the lowest PM ceram20Mn-150/900 to the highest PM ceram10Mn-150/700.

As may be noticed in Fig. 11, left, the curves $M \times T$ *vs. T* for ceram10Mn-150/700, ceram10Mn-150/500, and ceram5Mn-150/900 have very similar shapes that only slightly continue to grow with temperature for $T > 200$ K pointing out to relatively low contributions of the AFM phase(s). In contrast, the AFM phase contribution in ceram20Mn-900 is the largest. The extracted PM contributions, which we believe represent the (Ga, Mn)N phase, are shown in Fig. 11, right.

By using the earlier described procedure [7], one could roughly estimate the Mn-contents in the paramagnetic (Ga, Mn)N phase and the contents of the antiferromagnetic Mn_2SiO_4 by-product in four ceramics with the initial 5 and 10 at.% Mn-contents as well as give a very rough estimate for ceram20Mn-150/900. The estimates are shown in Table 4 for which the same comments apply as discussed earlier for Table 2.

It is clear that the sintering process results in the increased Mn-contents in the major phase (Ga, Mn)N, which is consistent with the discussed trends for the PM contributions in magnetization of the ceramics. Such an outcome suggests that during sintering some Mn-ions from the AFM phase(s) (*e.g.*, Mn_2SiO_4 or amorphous Mn–N–S–C species) in the nanopowders have diffused to the (Ga, Mn)N paramagnetic phase. A net effect is the observed relative decrease of the AFM contribution with a simultaneous increase of the PM contribution in the ceramics.

Regarding the estimations of the Mn-content in (Ga, Mn)N, we note the problem with exact weights of all the different phases, which limits the accuracy of such indirect determinations.

We recall that in three of our sintered samples at least one of the two diamagnetic phases, *i.e.*, γ-$Ga_2(O,N)_3$ or α-Ga_2O_3 was detected. One should also be aware of amorphous residual phases that could

be present though undetected by XRD. Because of these uncertainties we refrained from a more detailed analysis of the measured magnetization. This issue could partly be resolved with the help of XRD data. However, the crystallite texturing and peak broadening due to broad crystallite size distribution overwhelmingly added to the complexity of the XRD patterns and made our simulation trials of the effect of Mn substituting Ga on peak intensities futile. At the end, we express an opinion that the Mn-contents derived from the magnetic measurements constitute a solid base for comparative purposes and studying important trends.

4. Conclusions

Various Mn-doped gallium nitride nanopowders were prepared from a new bimetallic precursor system with a range of initial Mn-contents, 5–20 at.% *vs.* Ga, utilizing a two stage nitridation pyrolysis under an ammonia flow, *i.e.*, first stage at 150 °C followed by the second stage at 500, 700 or 900. The target doping of the GaN lattice with Mn was achieved at the relatively stable *ca.* 2–3 at.% Mn-content level irrespective of a wide range of applied precursors and conversion temperatures. Purposely, excessive quantities of manganese *vs.* GaN from the point of view of plausible Mn-doping levels were used. This and incomplete transamination chemistry in the system resulted in residual amorphous by-products which contained Mn and Si. The measurements of the nanopowders magnetic properties pointed out to the target paramagnetic (Ga, Mn)N phase with antiferromagnetic interactions among Mn-ions. There was also an additional magnetic component in total magnetization which could be satisfactorily assigned to the adventitious antiferromagnetic Mn_2SiO_4 that was assumed to form *via* a facile oxidation of the residual species upon powder exposure to air.

Five nanopowders prepared from various precursors were subjected to a high-pressure high-temperature sintering under conditions mimicking our successful no-additive sintering of pure gallium nitride nanopowders. The specific sintering parameters, 7 GPa, 1000 °C, 10 min, were selected to provide conditions suitable for nanocrystallite recrystallization. The products identified in the ceramics included the major gallium nitride-based phase (Ga, Mn)N and some crystalline residues formed from oxidation of the initially amorphous by-products present in the starting nanopowders. Interestingly, in the case of the highest Mn-content sample, where suitably high proportions of by-products were present, the average crystallite size of the (Ga, Mn)N phase was lower in the ceramics than in the related substrate nanopowder. This indicated a fine interplay between the nitride recrystallization and a diluent-type effect taking place during sintering. The estimated Mn-contents in (Ga, Mn)N of the sintered ceramics in the range *ca.* 3–5 at.% were, generally, significantly higher by a factor *ca.* 1.6 than in the substrate nanopowders. This was consistent with an overall advantageous impact of the high-pressure high-temperature sintering conditions on Mn-incorporation in the GaN lattice.

Acknowledgement

This work was supported by the Polish National Science Center, NCN, Grant No. 2011/01/B/ST5/06592.

References

[1] (a) T. Dietl, H. Ohno, Dilute ferromagnetic semiconductors: physics and spintronic structures, Rev. Mod. Phys. 86 (2014) 187–251;
(b) T. Jungwirth, J. Wunderlich, V. Novak, K. Olejnik, B.L. Gallagher, R.P. Campion, K.W. Edmonds, A.W. Rushforth, A.J. Ferguson, P. Nemec, Spin-dependent phenomena and device concepts explored in (Ga,Mn)As, Rev. Mod. Phys. 86 (2014) 855–896;
(c) A. Hirohata, K. Takanashi, Future perspectives for spintronic devices, J. Phys. D Appl. Phys. 47 (2014) 1–40;
(d) S.S. Khludkov, I.A. Prudaev, O.P. Tolbanov, Gallium nitride as a material for spintronics, Russ. Phys. J. 55 (2013) 903–909;
(e) R. Buonsanti, D.J. Milliron, Chemistry of doped colloidal nanocrystals, Chem. Mater. 25 (2013) 1305–1317.

[2] (a) M. Kaminska, S. Podsiadlo, P. Dominik, K. Wozniak, L. Dobrzycki, R. Jakiela, A. Barcz, M. Psoda, J. Mizera, R. Bacewicz, M. Zajac, A. Twardowski, New chemical method of obtaining thick $Ga_{1-x}Mn_xN$ layers: prospective spintronic material, Chem. Mater. 19 (2007) 3139–3143;
(b) S. Podsiadlo, T. Szyszko, W. Gebicki, J. Gosk, R. Bacewicz, L. Dobrzycki, K. Wozniak, M. Zajac, A. Twardowski, Synthesis of bulk $Ga_{1-x}Mn_xN$: a prospective spintronic material, Chem. 15 (2003) 4533–4535;
(c) A. Wolos, M. Palczewska, M. Zając, J. Gosk, M. Kaminska, A. Twardowski, M. Bockowski, I. Grzegory, S. Porowski, Optical and magnetic properties of Mn in bulk GaN, Phys. Rev. B 69 (2004) 1–7;
(d) M. Zając, J. Gosk, E. Grzanka, S. Stelmakh, M. Palczewska, A. Wysmołek, K. Korona, M. Kamińska, A. Twardowski, Ammonothermal synthesis of GaN doped with transition metal ions (Mn, Fe, Cr), J. Alloy. Compd. 456 (2008) 324–338.

[3] (a) J.F. Janik, M. Drygaś, C. Czosnek, M. Kamińska, M. Palczewska, R.T. Paine, Carbothermally-assisted aerosol synthesis of semiconducting materials in the system GaN/Mn, J. Phys. Chem. Solids 65 (2004) 639–645;
(b) J.B. Gosk, M. Drygas, J.F. Janik, M. Palczewska, R.T. Paine, A. Twardowski, Magnetic and optical properties of (GaMn)N nanocrystalline powder sprepared by the aerosol-assisted vapour phase synthesis and anaerobic imide route methods, J. Phys. D: Appl. Phys. 39 (2006) 3717–3725.

[4] (a) Z. Sofer, D. Sedmidubsky, S. Huber, J. Hejtmanek, A. Mackova, R. Fiala, Mn doped GaN thin films and nanoparticles, Int. J. Nanotechnol. 9 (2012) 809–824;
(b) Z. Sofer, D. Sedmidubsky, S. Huber, P. Simek, F. Sanek, O. Jankovsky, E. Gregorova, R. Fiala, S. Matejkova, M. Mikulics, Rapid thermal synthesis of GaN nanocrystals and nanodisks, J. Nanopart. Res. 15 (2013) 1411;
(c) Z. Ma, M.E. Jamer, E. Panaitescu, D. Heiman, L. Menon, Structure and magnetism of GaMnN nanowires synthesized with nonmagnetic catalyst, J. Magn. Magn. Mater. 394 (2015) 155–159;
(d) C. Mahendiran, T. Maiyalagan, P. Kannan, One-pot simple synthesis and characterisation of Mn^{2+}-doped GaN nanorods by RAPET method, J. Exp. Nanosci. 10 (2015) 859–867.

[5] D. Sedmidubsky, J. Leitner, Z. Sofer, Phase relations in the Ga–Mn–N system, J. Alloy Compd. 452 (2008) 105–109.

[6] (a) S. Podsiadlo, T. Szyszko, W. Gebicki, J. Gosk, R. Bacewicz, L. Dobrzycki, K. Wozniak, M. Zajac, A. Twardowski, Synthesis of bulk $Ga_{1-x}Mn_xN$: a prospective spintronic material, Chem. Mater. 15 (2003) 4533–4535;
(b) Y. Wei, J. Guo, D. Hou, S. Qiao, Preparation and properties of Mn-doped GaN powders, Solid State Commun. 148 (2008) 234–236;
(c) M.H. Ham, J.M. Myoung, Doping concentration dependence of ferromagnetic ordering in (Ga,Mn)N nanowires, Appl. Phys. Lett. 89 (2006) 173117.

[7] M. Drygas, J.F. Janik, M.M. Bucko, J. Gosk, A. Twardowski, Structural and magnetic properties of GaN/Mn nanopowders prepared by an anaerobic synthesis route, RSC Adv. 5 (2015) 37298–37313.

[8] (b) P.F. McMillan, Chemistry of materials under extreme high pressure-high-temperature conditions, Chem. Commun. 8 (2003) 919–923;
P.F. McMillan, High pressure synthesis of materials, in High pressure crystallography: from fundamental phenomena to technological applications, Book Series: NATO Science for Peace and Security Series B-Physics and Biophysics (2010); 373–383.

[9] (a) A. Escudero, F. Langenhorst, Chromiumin corporation into TiO_2 at high pressure, J. Solid State Chem. 190 (2012) 61–67;
(b) A. Escudero, F. Langenhorst, W.F. Muller, Aluminum solubility in TiO_2 rutileathigh pressure and experimental evidence for a $CaCl_2$-structured polymorph, Am. Miner. 97 (2012) 1075–1082.

[10] (a) S. Stelmakh, A. Swiderska-Sroda, G. Kalisz, S. Gierlotka, E. Grzanka, B. Palosz, M. Drygas, J.F. Janik, R.T. Paine, Microstructure and mechanical properties of GaN nanoceramics sintered under high-pressure-high-temperature conditions, in: Proceedings of the International Conference on Nanoscience and Technology, Basel, Switzerland, July 30–August 4, 2006, Institute of Physics Publishing :Philadelphia, PA, 2006;
(b) E. Grzanka, S. Stelmakh, S. Gierlotka, A. Swiderska- Sroda, G. Kalisz, B. Palosz, M. Drygas, J.F. Janik, R.T. Paine, In situ X-ray diffraction studies of distribution of strainduring simultaneous sintering of nanocrystalline GaN powder sunder high-pressure high-temperature conditions, in: European Powder Diffraction Conference, EPDIC-10, Geneva, Switzerland, September1-4, 2006, Z. Kristallogr. 26(2007) MS11-P92;
(c) J. Borysiuk, P. Caban, W. Strupinski, S. Gierlotka, S. Stelmakh, J.F. Janik, TEM investigations of GaN layers grown on silicon and sintered GaN nano-ceramic substrates, Cryst. Res. Technol. 42 (2007) 1291–1296-;
(d) J.F. Janik, M. Drygaś, C. Czosnek, B. Palosz, S. Gierlotka, S. Stelmakh, E. Grzanka, G. Kalisz, A. Świderska-Środa, M. Leszczyński, G. Nowak, R. Czernecki, A way to make sintered gallium nitride GaN, Polish Patent No. 210651, Feb. 29, 2012, WUP02/12.

[11] (a) Z. Krstic, V.D. Krstic, Silicon nitride: the engineering material of the future, J. Mater. Sci. 47 (2012) 535–552;
(b) H.M. Lee, K. Bharathi, D.K. Kim, Processing and characterization of aluminum nitride ceramics for high thermal conductivity, Adv. Eng. Mater. 16 (2014) 655–669;
(c) K. Lu, Sintering of nanoceramics, Int. Mater. Rev. 53 (2008) 21–38;

(d) U.W. Blaess, T. Barsukova, M.R. Schwarz, A. Köhler, C. Schimpf, I.A. Petrusha, U. Mühle, D. Rafaja, E. Kroke, Bulk titaniumnitride ceramics—significant enhancement of hardness by silicon nitride addition, nano structuring and high pressures intering, J. Eur. Ceram. Soc. 35 (2015) 2733–2744;
(e) T. Suehiro, N. Hirosaki, K. Komeya, Synthesis and sintering properties of aluminiumnitridenanopowderpreparedbythegas-reduction-nitridation method, Nano Technol. 14 (2003) 487–491;
(f) O. Jankovski, D. Sedmidubsky, S. Huber, P. Simek, Z. Sofer, Synthesis, magnetic and transport properties of oxygen-free CrN ceramics, J. Eur. Ceram. Soc. 34 (2014) 4131–4136.

[12] (a) J.F. Janik, R.L. Wells, Gallium imide,$\{Ga(NH)_{3/2}\}_n$,a new polymeric precursor for gallium nitride powders, Chem. Mater. 8 (1996) 2708–2711;
(b) J.F. Janik, R.L. Wells, J.L. Coffer, J.V. St. John, W.T. Pennington, G.L. Schimek, Nanocrystalline aluminum nitride and aluminum/gallium nitride nanocomposites via transamination of $[M(NMe_2)_3]_2$, M = Al, Al/Ga (1/1), Chem. Mater. 10 (1998) 1613–1622.

[13] (a) D.C. Bradley, M.B. Hursthouse, K.M.A. Malik, R. Moseler, The crystal structure of bis(hexamethyldisilylamido) manganese, Transit. Met. Chem. 3 (1978) 253–254;
(b) H. Chen, M.M. Olmstead, D.C. Pestana, P.P. Power, Reactions of low-coordinate transition-metal amides with secondary phosphanes and arsanes: synthesis, structural, and spectroscopic studies of $[M\{N(SiMe_3)_2\}(\mu\text{-}PMes_2)]_2$(M = Mn,Fe),$[Mn\{N(SiMe_3)_2\}(\mu\text{-}AsMes_2)]_2$, and $Mes_2AsAsMes_2$, Inorg. Chem. 30 (1991) 1783–1787.

[14] J.W. Hwang, J.P. Campbell, J. Kozubowski, S.A. Hanson, J.F. Evans, W.L. Gladfelter, Topochemical control in the solid-state conversion of cyclotrigallazane into nanocrystalline gallium nitride, Chem. Mater. 7 (1995) 517–525.

[15] R. Pompe, Preparation and TG-DTA analysis of manganese silicon nitride, Thermochim. Acta 16 (1976) 295–300.

[16] (a) B.A. Fusenko, Synthesis of new high-pressure silicate garnets $Mn_3M_2Si_3O_{12}$ (M = V, Mn, Ga), Dokl. Akad. Nauk SSSR 268 (1983) 421–424;
(b) T. Arlt, T. Armbruster, R. Miletich, P. Ulmer, T. Peters, High pressure single-crystal synthesis, structure and compressibility of the garnet $Mn_3^{2+}Mn_2^{3+}[SiO_4]_3$, Phys. Chem. Miner. 26 (1998) 100–106.

[17] (a) C.A. Deshmane, J.B. Jasinski, M.A. Carreo, Thermally stable nanocrystalline mesoporous gallium oxide phases, Eur. J. Inorg. Chem. 22 (2009) 3275–3281;
(b) Y. Masubuchi, Synthesis, structure and properties of new functional oxynitride ceramics, J. Ceram. Soc. Jpn. 121 (2013) 142–149;
(c) M. Martin, R. Dronskowski, J. Janek, K.D. Becker, D. Roehrens, J. Brendt, M.W. Lumey, L. Nagarajan, I. Valov, A. Borger, Thermodynamics, structure and kinetics in the system Ga–O–N, Prog. Solid State Chem. 37 (2009) 132–152;
(d) H. Huppertz, S.A. Hering, C.E. Zvoriste, S. Lauterbach, O. Oeckler, R. Riedel, I. Kinski, High-pressure synthesis, electron energy-loss spectroscopy investigations, and single crystal structure determination of a spinel-type gallium oxonitride $Ga_{2.79}\square_{0.21}(O_{3.05}N_{0.76}\square_{0.19})$, Chem. Mater. 21 (2009) 2101–2107.

[18] (a) R.P. Santoro, R.E. Newnham, S. Nomura, Magnetic properties of Mn_2SiO_4 and Fe_2SiO_4, J. Phys. Chem. Solids 27 (1966) 655–666;
(b) W. Lottermoser, H. Fuess, Magnetic structure of the orthosilicates Mn_2SiO_4 and Co_2SiO_4, Phys. Status Solidi (a) 109 (1988) 589–595;
(c) I.S. Hagemann, P.G. Khalifah, A.P. Ramirez, R.J. Cava, Geometric magnetic frustration in olivines, Phys. Rev. B 62 (2000) R771–R774.